ADVANCED ENGINEERING MATERIALS
www.aem-journal.com

Unveiling 3D Morphology of Multiscale Micro-Nanosilver Sintering for Advanced Electronics Manufacturing by Ptychographic X-ray Nanotomography

Yu-Chung Lin, Xiaoyang Liu, Kang Wei Chou, Esther H. R. Tsai, Chonghang Zhao, Mirko Holler, Ana Diaz, Stanislas Petrash, and Yu-chen Karen Chen-Wiegart**

The sintering processing–structure–property relationship of a multiscale silver materials is investigated: microparticles with nanofeatures, particularly on their three-dimensional (3D) morphology. The target application is to replace conventional lead-based solders in advanced electronic manufacturing. Unlike lead-based solders, silver powders are suited to satisfy increasingly demanding mechanical, electrical, and thermal requirements, meanwhile being free of health effect. Sintering the material at a low temperature and without applied pressure are desirable conditions, which results in a preferred use of silver nanoparticles, as nanofeatures have higher driving force to sinter with the decrease in particle size. However, nanosized powders present potential health/environmental effects. To address the trade-off between the benefits and shortcomings of nano-versus microparticles, this work studies a novel multiscale silver paste, namely micron-sized powders with nanosized features. To get quantitative 3D visualization of micro- and nanoscale features, ptychographic X-ray computed nanotomography is applied. The correlations between conditions (thermal aging, pressure, and substrate metallization), mechanical properties, and morphological parameters are established. Using novel 3D X-ray nanoimaging technique, it is demonstrated that one can design multiscale materials while balancing complex demands required in advanced electronics manufacturing and research directions in materials design and characterization.

1. Introduction

Advanced materials design and processing plays a critical role in electronics manufacturing, with electronics packaging being one of the key areas. A common method of component attachment in electronics industry is the use of lead (Pb)-based eutectic alloys for binding adjacent layers together to form 3D architectures. However, there are many environmental, health, and regulatory challenges associated with the use of Pb-based alloys in advanced electronics and beyond.[1] Some lead-free alternatives such as Zn-, Au-, or Bi-based alloys have disadvantages including poor solderability, weak corrosion resistance, and causing damages in devices.[2,3] Therefore, there has been growing fundamental, multidisciplinary research effort to design new lead-free materials for effective interfacial joining, driven by the need to develop the next-generation electronics packaging and processing strategies.

Silver (Ag) paste that is based on sintering micron- and nanoscale Ag powder became an attractive potential alternative, because Ag paste has been shown to bond

Y.-C. Lin, X. Liu, C. Zhao, Prof. Y.-c.K. Chen-Wiegart
Department of Materials Science and Chemical Engineering
Stony Brook University
Stony Brook, NY 11794, USA
E-mail: karen.chen-wiegart@stonybrook.edu

Dr. K. W. Chou
Henkel Adhesive Technologies
Global Innovation Research
Advanced Characterization Group
Hendel Ibérica S.A. Campus UAB, Edificio Eureka 08193, Bellaterra

Dr. E. H. R. Tsai, Dr. M. Holler, Dr. A. Diaz
Swiss Light Source
Paul Scherrer Institute
Forschungsstrasse 111, CH-5232 Villigen, Switzerland

Dr. E. H. R. Tsai
Center for Functional Nanomaterials
Brookhaven National Laboratory
Upton, NY 11973, USA

Dr. S. Petrash
Henkel Adhesive Technologies
Global Innovation Research
Advanced Characterization Group Henkel Corporation
Bridgewater, NJ 08807, USA
E-mail: stan.petrash@henkel.com

Prof. Y.-c.K. Chen-Wiegart
National Synchrotron Light Source II
Brookhaven National Laboratory
Upton, NY 11973, USA

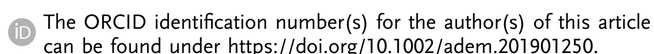
The ORCID identification number(s) for the author(s) of this article can be found under https://doi.org/10.1002/adem.201901250.

DOI: 10.1002/adem.201901250

 © 2020 WILEY-VCH Verlag GmbH & Co. KGaA, Weinheim

and cure at a relatively low temperature, 200–300 °C.[4,5] Sintering is a process that joins interfaces of materials by various diffusion routes at a temperature that is sufficiently high to allow diffusion to occur, but yet below the material's melting point of the sintering materials.[6] The operating temperature, which is lower than the melting point of the joining materials, enables creating joints by sintering Ag particles without generating liquid phases. This has a great advantage as it eliminates the resolidification procedure in the process, which is highly complex and can generate secondary phases via kinetic-limited processes, which are challenging to control precisely.

The conventional Ag sintering process involves pressure-assisted sintering of micron-scale powders,[7–9] driving up the processing constraints and cost. Developing a pressureless Ag sintering process was thus inspired, where the use of micron-sized metallic particles with nanosized features plays a key role in removing the required pressure in materials processing. The presence of nanosized features resulted in a higher surface area per volume; thus, the intrinsic sintering driving force becomes higher, lowering the required processing temperature and pressure. Furthermore, sintering Ag particles with relatively small size in one dimension provides enhanced properties including good shear strength and electric conductivities.[10] In contrast, the particles are still micron-sized in other two dimensions, which avoids the toxicity issues associated with nanoparticles.

Prior studies focused on characterizing the mechanical properties including shear or tensile stress of the sintered Ag with different sintering time, pressure, temperature, and aging time using X-ray diffraction, scanning electron microscopy, and X-ray tomography.[11,12] Milhet et al.[13] studied micron Ag paste and quantitatively analyzed the connectivity, pore geometry, pore spatial distribution, and density evolution with different aging temperature of the porous sintered Ag to study the growth, Ostwald ripening, and clustering of the pores using in situ X-ray tomography. Suzuki et al.[14] used finite element analysis (FEA) to simulate the mechanical behavior based on 3D microstructures obtained from serial focused ion beam scanning electron microscopy (FIB-SEM) cross-sectional images. In addition, the substrate and die metallization were correlated with the mechanical properties, microstructural characterization, and long-term reliability. Chua and Siow studied the direct bond copper (DBC) substrate without metallization and observed the formation of an additional layer of copper (Cu) oxide.[15] Other research studied the influence of different metallization layers such as PdAg, Au, and Ag, which generally exhibited good initial mechanical properties, i.e., die shear test values above 15 MPa. However, after sintering, only the Ag metallization sample conformed to the required die shear test values.[15,16] For gold (Au) metallization layer, the changes in morphology and interface included voids formation or a depletion layer would weaken the mechanical properties.[17,18] Although prior characterization on these structures provided valuable information, further analysis in 3D to visualize the interfaces and the layer-to-layer interaction is required to further understand the processing–structure–property of this multilayer structure.[19]

Ptychographic X-ray computed tomography (PXCT)[20,21] is a novel high-resolution 3D microscopy method. As a lensless coherent imaging method, the resolution of PXCT is not limited by the X-ray optics and the reconstructed images directly and quantitatively represent the 3D distribution of the electron density of the structure. Applications of PXCT have been demonstrated in various important fields including biomedicine to quantify detailed structures within a bone[19] and electronics[22] to reveal the finest details of a computer chip. In this work, PXCT was applied to study a novel sintered Ag made of micron-sized metallic particles with nanosized features which play a key role in pressureless sintering during materials processing. Furthermore, the interface between sintered Ag, substrate, and metallization layer were visualized by PXCT with quantitative 3D electron-density mapping. Specifically, the effects of Au metallization, sintering pressure, and postprocessing thermal aging on the 3D morphological parameters were investigated in conjunction with the die attachment mechanical properties. The critical 3D morphological parameters were quantified, including the feature size distribution of the different phases and spatially resolved porosity as a function of metallization substrates, sintering pressure and thermal aging conditions, and curvature distribution of Ag surface. Overall, the work provides an understanding of the formation of important features including porosity gradient, voids, and depletion layers at different layers, and sheds the light on understanding micro-nanomaterials, electronics, and thin films for the processing–structure–property correlation utilizing PXCT.

2. Results and Discussion

The sintering and aging conditions are shown in **Table 1**, which are chosen to be consistent with processing parameters used in electronics die attach applications as well as in relevant studies[13,23] (see Supporting Information for detailed sample preparation). The effects of different conditions—pressure, aging, and metallization—on the 3D morphology were investigated, with a focus on the 3D morphology at the interface between nano-Ag

Table 1. Sample preparation parameters to study the effects of the Au metallization, sintering conditions, and aging condition in the 3D morphology of nanosilvers used in die attachments.

Sample	Metallization	Sintering condition		Aging temperature and time	Abbreviation
		Sintering pressure and time	Sintering temperature and time		
A	No	10 MPa, 5 min	250 °C, 5 min	24 h, 250 °C	nAu—P—A
B	Au	10 MPa, 5 min	250 °C, 5 min	24 h, 250 °C	Au—P—A
C	Au	10 MPa, 5 min	250 °C, 5 min	No	Au—P—nA
D	Au	No	250 °C, 60 min	No	Au—nP—nA

© 2020 WILEY-VCH Verlag GmbH & Co. KGaA, Weinheim

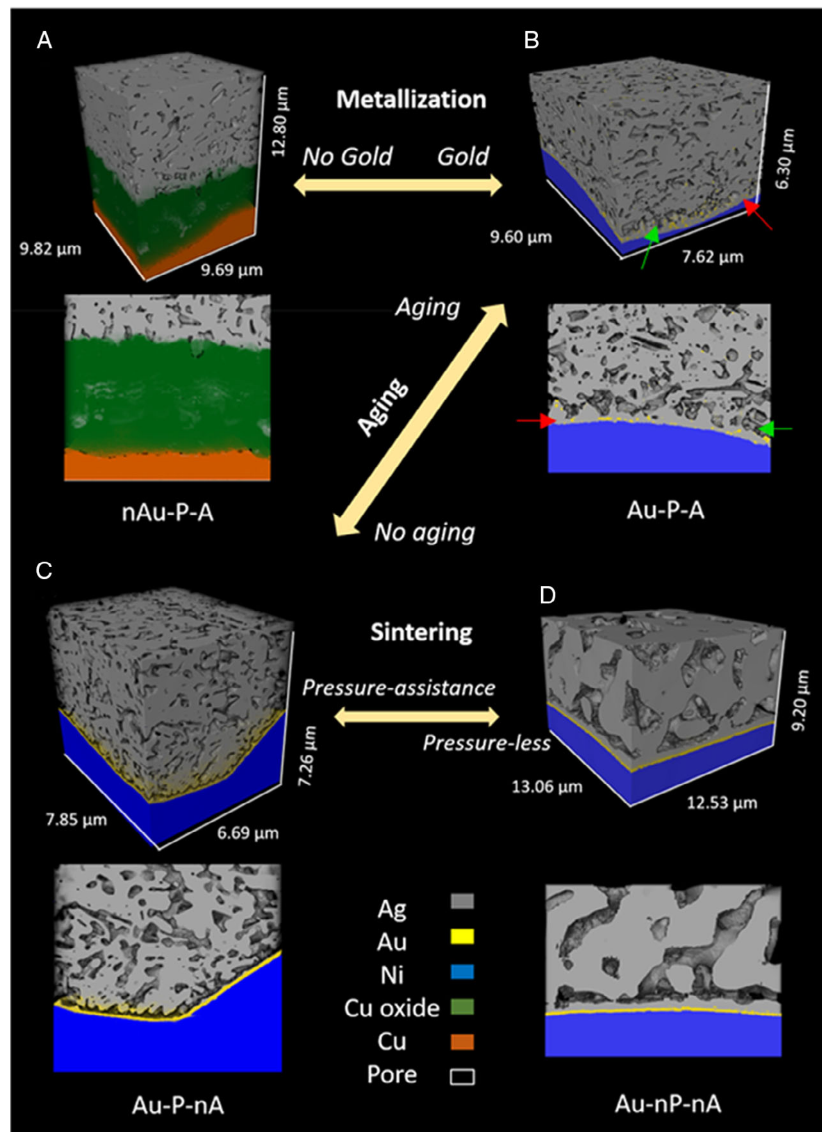

Figure 1. 3D segmented reconstructions of sintered samples by PXCT showing phase structure: A) sample A: nAu—P—A; B) sample B: Au—P—A; C) sample C: Au—P—nA; and D) sample D: Au—nP—nA; red arrows indicate a dense Ag layer and green arrows indicate a region higher porosity as a result of Au metallization layer. The opacity of the Cu oxide phase was altered for visualization. Videos of the samples can be viewed in Supporting Information.

sintered powder and the substrate interface. **Figure 1** shows the 3D segmented and cropped reconstructions of PXCT and the corresponding cross-sectional view of the segmented volumes. Different colors represent different phases as shown in Figure 1. The effects of different controlled parameters including Au metallization, aging, and pressure are discussed later.

The effect of Au metallization can be seen by comparing Figure 1A (sample A without Au metallization) and Figure 1B (sample B with Au metallization). In sample B, the Au metallization layer shown in yellow between the DBC substrate and sintered Ag layer shown in gray appeared to act as a passivation layer to prevent the oxygen from diffusing through the porous Ag to react with the DBC substrate. This is evident from the fact that without such Au metallization on the substrate, sample A forms an additional phase shown as green at the interface of Ag and DBC substrate.

This phase is clearly visible in **Figure 2**, which shows X-ray projection images collected from the same sample A measured by ptychography and X-ray fluorescence. This phase was previously identified to be of Cu oxide using energy-dispersive electron spectroscopy (EDS). It showed that aging a similar sintered Ag sample without metallization layer at 300 °C in air will expose the sample in rich oxygen environment, leading to the formation of a thick Cu oxide layer.[24,25] Literature also showed that the Cu oxide can further interdiffuse with the Ag phase after thermal annealing under 300 °C for 50 h. This Cu oxide–Ag interdiffusion leads to an interconnected “interlock” structure between the Cu substrate and Ag phases and therefore

© 2020 WILEY-VCH Verlag GmbH & Co. KGaA, Weinheim

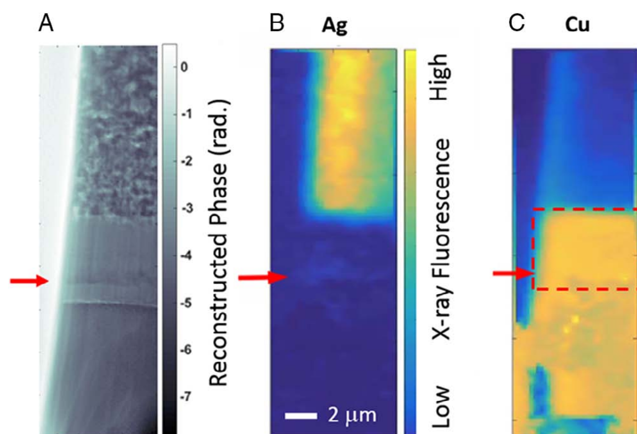

Figure 2. X-ray projection images collected from sample A. The same vertical location is shown with a red arrow as a guide for the eye. A) Ptychographic projection of a region of interest within the sample. B) Ag and C) Cu X-ray fluorescence images of the same region, showing an interdiffusion Cu-rich layer (dashed frame) due to the lack of Au layer. Some additional Cu signals were observed on the exterior region, likely due to the background signals of the sample mount.

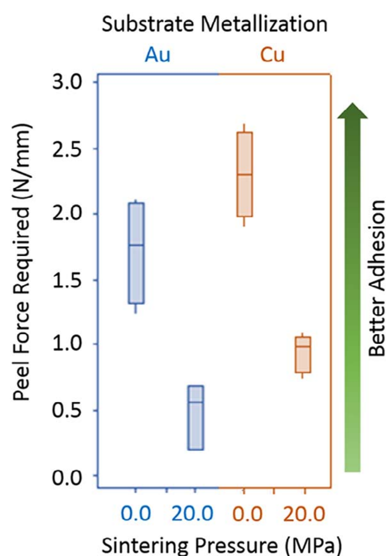

Figure 3. Peel data (in N mm^{-1}) on sintered Ag samples, showing the effect of substrate metallization and sintering pressure.

results in a better adhesion of Ag to the substrate. The enhancement of the adhesion is evident from **Figure 3**, which shows better adhesion values for Cu substrate (≈1 N mm^{-1}) versus Au-metallized substrate (≈0.5 N mm^{-1}).[15] However, after a long-term aging, the thickness of the Cu oxide layer tends to increase, and the joint will become weaker, due to the mismatch of the thermal expansion coefficients between Cu, Cu oxide, and sintered Ag.

Aged at 250 °C for 24 h, sample B formed a denser Ag layer with lower porosity (shown as gray, indicated with red arrows) when contacting with Au layer (shown as yellow) as shown in Figure 1B; this layer also showed interdiffusion between Ag and Au. Right above the denser Ag layer, a layer with higher porosity (shown in black, indicated with green arrows) was also identified. In contrast, without the thermal aging (sample C), the density of porous Ag structure was distributed uniformly, without forming a denser layer at the interface with the Au metallization (Figure 1C). Muralidharan et al. found that a similar sample aged at 300 °C for 24 h formed a void-free layer with adjacent "depletion" layer and the growth of the thickness of this void-free layer was reported to be proportional to the aging time.[26] Meanwhile, the depletion layer with higher porosity was found to gradually increase with increased aging time. The formation of this depletion layer with higher porosity is consistent with Kirkendall effect. This phenomenon had been reported in diffusion couple of Ag–Au alloys at 875 °C,[27–29] caused by the different diffusivities between Ag and Au in their interdiffusion. Such depletion layer near the interface can potentially harm the mechanical properties of the materials. Chen et al. found that the void-free layer and depletion layer were not seen after 1000 h of aging at 300 °C.[24] However, aging the sample for 24 h is not long enough to eliminate the depletion layer; thus, both the depletion and void free layer were found in sample B.

Application of pressure during sintering appears to have a significant effect on 3D morphology of sintered Ag. Comparison between Figure 1C (sample C with pressure) and Figure 1D (sample D without pressure) showed much larger interconnects in Ag network for the sample sintered with no pressure. The pressure-sintered sample showed considerably smaller pore size, but with thinner sample interconnections. As a result, if pressure is applied during sintering of Ag powders, the adhesion is significantly reduced (Figure 3). Two effects can contribute to this result: First, the larger Ag ligament interconnects and pore sizes in sample D could be large due to the higher sintering time needed for pressureless sintering condition. Second, the pressure may disrupt the "stacking" of the flat Ag particles. This particle "stacking" appears to be responsible for thicker interconnects in sample C, whereas in sample D, the pressure applied during sintering appears to disrupt the stacking arrangement resulting in finer structure with thinner interconnects.

The phase distribution profiles of pore, Ni, Ag, Au, Cu, and Cu oxide for each of the samples correlated with the interface morphology are shown in **Figure 4**. The distance was measured relative to the Ag substrate interface. The data provide quantitative information about the 3D sample morphology, and a more accurate representation of the sample, compared with information obtained from analysis of 2D cross-section obtained by the FIB-SEM technique.

Figure 4 showed that in sample A without Au layer, Cu oxide (shown in green) formed and diffused into the Ag layer (shown by the green line). Because Cu oxide is an insulator, the electrical conductivity of the materials would be reduced. In contrast, in sample B which had an Au metallization layer given by the magenta line in Figure 4C, no Cu oxide was formed at the interface because Au metallization and Ni layer prevented the formation of Cu oxide. Moreover, in Figure 4C, the phase volume fraction of Ag and Au increased together indicating that the Ag–Au interdiffusion (indicated by black arrows) occurred at the interface where the Au and Ag layers were directly in contact. Above the Ag–Au interdiffusion layer, the Ag phase volume fraction decreased from ≈70% to ≈50%, and the porosity increased from ≈25% to ≈50%, which indicate the formation of a

© 2020 WILEY-VCH Verlag GmbH & Co. KGaA, Weinheim

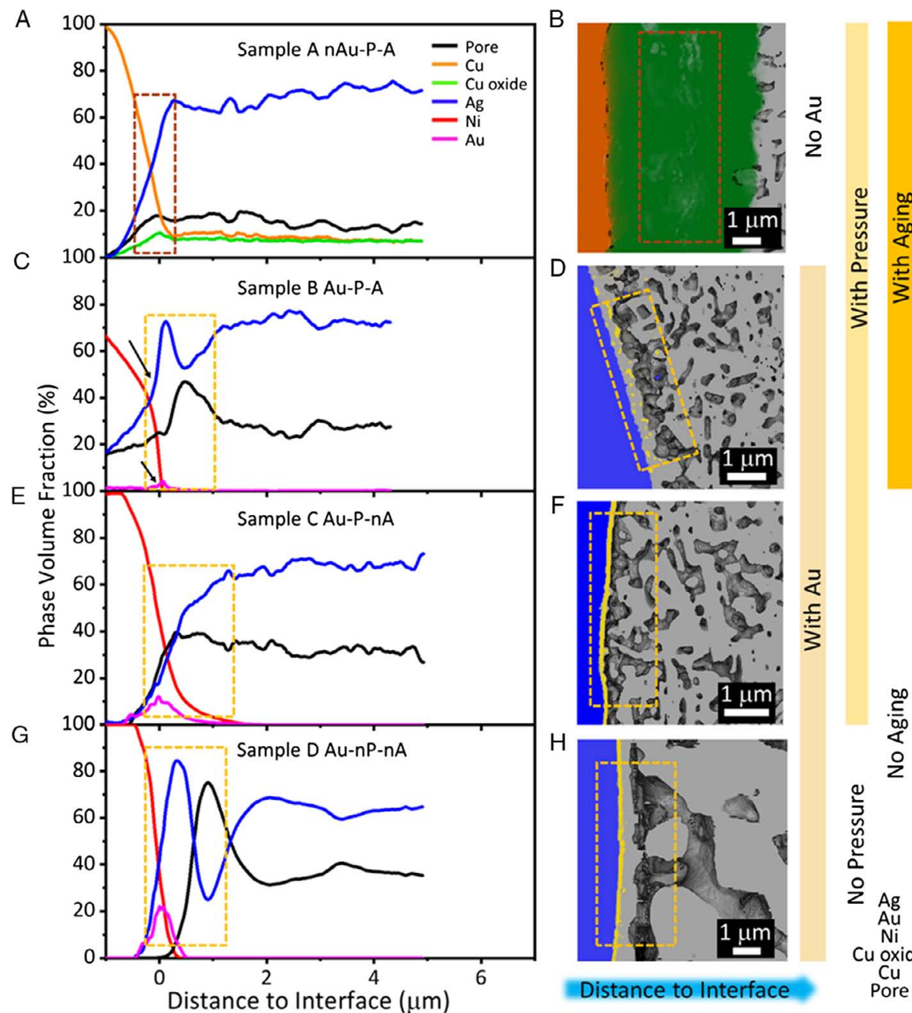

Figure 4. Quantification of phase distribution profiles correlated as a function of die attachment depth with corresponding interface morphology from cross-sectional view of segmented 3D volumes: A,B) sample A: nAu—P—A; C,D) sample B: Au—P—A; E,F) sample C: Au—P—nA; G,H) sample D: Au—nP—nA. Black arrows in part (C) indicate that when Au and Ag layers are directly in contact, the volume fraction of Ag and Au increases together likely due to interdiffusion.

"depletion layer" of Ag. This phenomenon may be caused because the diffusivity of Ag was higher than Au; as a result, the Ag diffused faster to the Au metallization layer, creating voids formed by Kirkendall effect.[30,31] This increased porosity at the interface is visualized in Figure 4D.

Figure 4 shows the phase volume fraction profiles of each elements and a direct visualization at the interface of sample C (Au—P—nA). Compared with sample B which was measured after an aging process, the Au profile in sample C is compact and obvious as shown quantitatively in Figure 4E, and sample C had a denser and distinct Au layer as shown in Figure 4F; this indicates that Au and Ag did not interdiffuse during the sintering process and the interdiffusion between Ag and Au in sample B was a result of the aging process. In addition, sample C showed a relatively uniform distribution of porosity (≈40%) throughout the Ag layer. Therefore, sintering process did not promote the interdiffusion between Au and Ag, but aging process will decrease the long-term stability and reduce the Ag adhesion to the Au-metallized substrate by forming pores at the interface between Au and Ag (Figure 3).

The effect of applied pressure during sintering process has been studied by comparing samples C (with pressure) and D (without pressure) as shown in Figure 4. For sample D, a longer sintering time was necessary to ensure structural integrity as the sintering was conducted without applied pressure; as a result, the coarsening of the structure was observed driven by minimizing the surface energy in porous media. At the interface, as the sintering time is much longer than sample C, the Ag would migrate to the Au layer. The depletion layer was formed after sintering process where the volume fraction of Ag decreased, and porosity increased.

The quantitative analysis of pore and Ag size distribution of samples with different control parameters is shown in **Figure 5**A. Sample A without Au layer had a pore size similar to sample B with Au layer. However, the Ag feature size of sample B was much smaller than that of sample A. The results indicated that

© 2020 WILEY-VCH Verlag GmbH & Co. KGaA, Weinheim

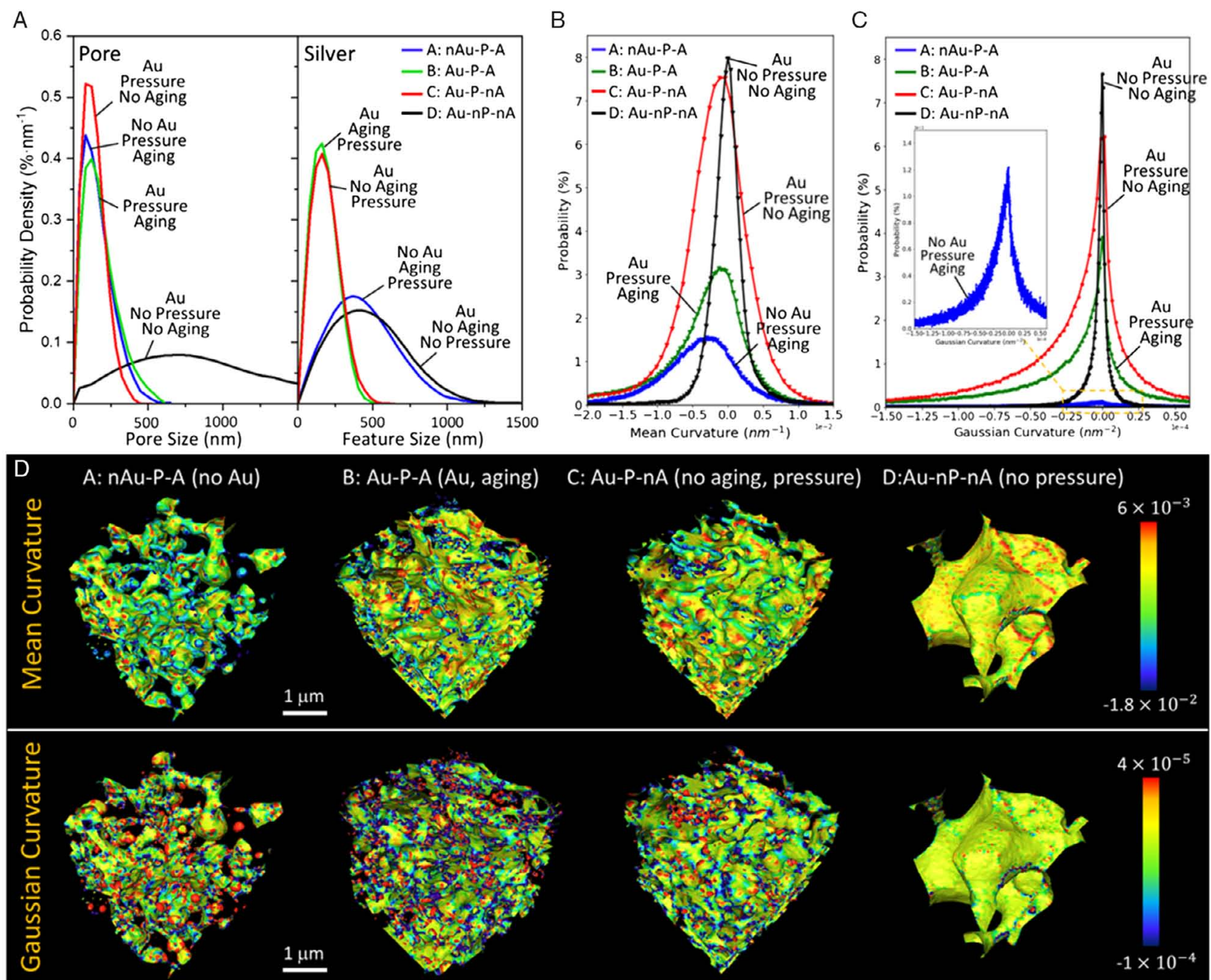

Figure 5. A) Feature size distribution of Ag and pore size distribution comparison between samples with different control parameters. B) Histogram of the mean curvature ($H = (K_1 + K_2)/2$) on Ag phase. C) Histogram of the Gaussian curvature ($K = K_1K_2$) on Ag phase. D) 3D visualization of Gaussian and mean curvature comparison for different control parameters.

the Au layer can hinder the migration between the sintered Ag and Cu and lead to the uniform structure of Ag size. In addition, the Ag feature size distribution in sample A was much broader than that of sample B. Furthermore, comparing with sample D (Au—nP—nA) while sintering without the pressure, the Au layer still cannot prevent Ag and pore growth.

The Ag size distribution did not show significant differences in samples with and without aging conditions between samples B and C. The pore size of sample B was larger than that of sample C due to aging effect. The pore size distribution of sample B showed a broader distribution compared with sample C. Under pressure-assisted sintering condition with Au layer, aging would affect the width of pore size distribution but not the size of Ag as shown in samples B and C. The aging also affected the migration of Ag that caused a depletion zone with high porosity in the middle of the Ag layer as in sample B.

Without pressure-assisted sintering, the sample D showed both broader Ag and pore-size distribution, with larger average Ag and pore size. However, for sample C with 5 min pressure sintering process, the Ag and pore size were much smaller than that of sample D. Pressure-assisted sintering was not ideal in IC manufacturing, and this study indicated that for this particular Ag pressureless sintering created larger interconnects (Figure 1). This is consistent with the longer time that is required to sinter the sample without the applied pressure. According to the previous study, while sintering for a longer time, the diffusion of the Ag would lead to coarsening and densification of Ag.[32]

It is known that the different curvatures in 3D structure lead to a chemical potential difference, which drives mass transportation and morphological evolution, including sintering. Therefore, studying the curvature difference at the interface is important. Figure 5 shows the histogram of mean (H) and Gaussian (K) surface curvature on Ag phase and correlated 3D visualization of different samples. Comparing the mean curvature of samples A and B, both of them showed that the majority were negative,

© 2020 WILEY-VCH Verlag GmbH & Co. KGaA, Weinheim

meaning that the surface of Ag had more concave points with lower chemical potential. But the mean curvature of sample B with Au metallization showed a narrower distribution with full width at half maximum (FWHM) at 0.00789 nm^{-1} (Table S1, Supporting Information); in addition, both mean and Gaussian curvature distributions were closer to 0 meaning that the surface shape of sample B with Au metallization contains more plane-like or saddle-point-like features. This type of structure would be closer to equilibrium, with less tendency to further evolve, likely caused by the densification process.

The mean and Gaussian curvatures of samples B and C were compared to study the influence of aging. The FWHM of the mean curvature in sample B was 0.00789 nm^{-1}, which was smaller than that of sample C at 0.00822 nm^{-1} (Table S1, Supporting Information). Therefore, sample B with aging presented a narrower mean curvature range, which means that the aging process further smoothed the surface of Ag particles. Lastly, when sintering with pressure, as was done in sample C, the driving force included external stress and intrinsic curvature-driven stress. Comparing samples C and D, sample C with pressure had lower average (−0.00245 nm^{-1}) and median (−7E-07 nm^{-1}) value of mean curvature with more concavities at the Ag surface.

3. Conclusion

We studied the 3D morphology for nano-Ag sintering process with controlled parameters: presence or absence of pressure during sintering, aging, and substrate metallization. A quantitative 3D morphological analysis was conducted, including the determination of the material phase profile in the direction perpendicular to the interface, calculation of feature size distribution, and 3D volume rendering. The 3D volume rendering showed that the sample without Au metallization formed an additional phase of Cu oxide. The samples with aging condition or pressureless sintering (sintering for longer duration) exhibited a void-free layer right at the Au/Ag interface, followed by an Ag depletion layer. The sample with pressure-assisted sintering, Au metallization, and without aging showed a uniform density profile of sintered Ag. Qualitatively, this sample showed both smaller pore and sintered Ag cluster size, compared with the sample sintered without pressure, with Au surface metallization and without aging. Moreover, in the analysis of phase distribution profile and feature size distribution, we quantified the joints interface properties and the morphological feature at the interface. Lastly, the curvature analysis of the Ag surface indicated the influence of control parameters on the chemical potential, which affected the kinetics of sintering process.

The results indicated that the pressureless sintering without Au metallization of the interface provides the best initial quality of Ag film in the initial state. Somewhat surprisingly, thermal aging did not increase the overall numerical density of Ag film. Instead, the Ag and Au interdiffused and formed a depletion layer, likely contributing to a weaker adhesion strength.

In this research, synchrotron PXCT provided the detailed and quantitative information of 3D microstructure to demonstrate the joints interface properties in aging, Au metallization, and pressure parameter. This work sheds light on the mechanisms of potential degradation mechanisms in sintered Ag powders for die attachment. The promise of using PXCT as an advanced 3D imaging tool for examining new materials in semiconductor design and processing was also demonstrated. Furthermore, the electrical conductivity of the materials after sintering and aging process is of great interest for future research.

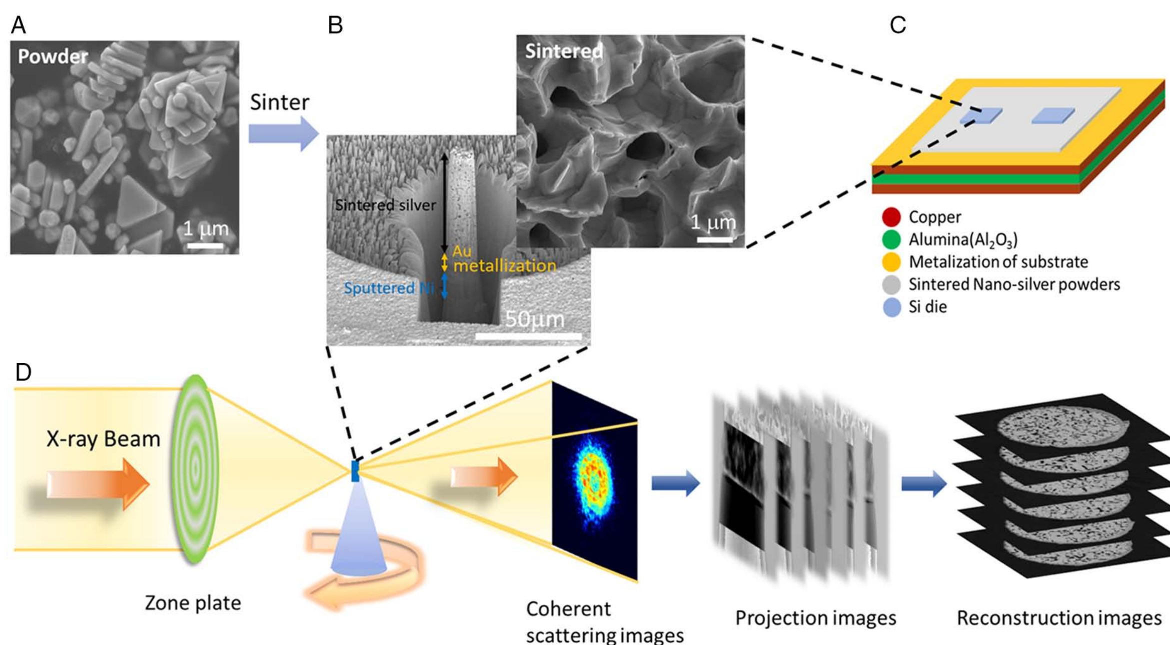

Figure 6. A) Surface morphology of Ag powder. B) Left: cross-section profile of sintered Ag porous structure and bonding with Au metallization; right: surface morphology of sintered Ag. C) Schematic diagram showing the layer structure of sintered Ag. D) Schematic diagram of PXCT setup.

 © 2020 WILEY-VCH Verlag GmbH & Co. KGaA, Weinheim

4. Experimental Section

Four samples were prepared for the high-resolution PXCT measurements. For sample A without an Au metallization layer, Ag powders (Henkel Belgium NV) were printed on the DBC substrate with a total thickness of 75 μm. A $1.8 \times 1.8\,cm^2$ die was attached on the Ag layer for further sintering process by annealing. For the remaining three samples, a nickel (Ni) metallization layer was first printed on the DBC substrates, then the Au metallization layer was applied prior to the Ag layer (**Figure 6**C). The pristine nano-Ag powder and sintered nano-Ag structure are shown in Figure 6. The samples were milled into a cylinder with diameter of 14–16 μm by FIB followed by a lift-out process[33] (Figure 6B) and were finally placed on a special sample mount[34] for PXCT measurements,[20,35] which were performed at the cSAXS beamline (X12SA, Figure 6D) at the Swiss Light Source, Paul Scherrer Institute (see Supporting Information for experiment).[22] After collecting the data, the central region in each of the 3D reconstruction image stack was cropped for further analysis. Different materials in the sample were then segmented based on their density difference shown in the grayscale histogram, using Avizo software (FEI, Version 9.4, see Supporting Information for detailed segmentation and quantification process). The phases include Cu, Cu oxide, Ni, Au, Ag, and pore (air). The adhesion test was conducted by performing 90° peel test. The peel speed of $8\,mm\,s^{-1}$ was used for samples.

Supporting Information

Supporting Information is available from the Wiley Online Library or from the author.

Acknowledgements

Y.C.L. and X.L. contributed equally to this work. We acknowledge the Swiss Light Source at the Paul Scherrer Institute, Villigen, Switzerland for provision of synchrotron radiation beamtime at beamline cSAXS–X12SA: coherent small-angle X-ray scattering. E.H.R.T. was supported by the Swiss National Science Foundation (SNSF) under grant numbers 200021_152554 and 200020_169623. This research used resources of the National Synchrotron Light Source II, a US Department of Energy (DOE) Office of Science User Facility operated for the DOE Office of Science by Brookhaven National Laboratory under contract no. DE-SC0012704. This research used resources of the Center for Functional Nanomaterials, which is a US DOE Office of Science Facility, at Brookhaven National Laboratory under contract no. DE-SC0012704. We also acknowledge the support by the Department of Materials Science and Chemical Engineering, the College of Engineering and Applied Sciences, and the Stony Brook University. We would like to acknowledge Liesbeth Theunissen and Anja Henckens from Henkel Belgium NV for inspiring this work, helpful discussion, and the adhesion data.

Conflict of Interest

The authors declare no conflict of interest.

Keywords

computed nanotomography, porous, ptychography, silver paste, tomography

Received: October 15, 2019
Revised: January 11, 2020
Published online:

[1] W. J. Plumbridge, R. J. Matela, A. Westwater, *Structural Integrity and Reliability in Electronics: Enhancing Performance in a Lead-Free Environment*, Kluwer Academic Publishers, Dordrecht **2003**.
[2] G. S. Jeong, D. H. Baek, H. C. Jung, J. H. Song, J. H. Moon, S. W. Hong, I. Y. Kim, S. H. Lee, *Nat. Commun.* **2012**, *3*, 977.
[3] C. Chen, H. M. Tong, K. N. Tu, *Annu. Rev. Mater. Res.* **2010**, *40*, 531.
[4] E. Ide, S. Angata, A. Hirose, K. F. Kobayashi, *Acta Mater.* **2005**, *53*, 2385.
[5] A. Hu, J. Y. Guo, H. Alarifi, G. Patane, Y. Zhou, G. Compagnini, C. X. Xu, *Appl. Phys. Lett.* **2010**, *97*, 153117.
[6] S. M. A. Robert, W. Balluffi, W. Craig Carter, *Kinetics Materials*, Wiley, New Jersey **2005**.
[7] T. Wang, X. Chen, G. Q. Lu, G. Y. Lei, *J. Electron. Mater.* **2007**, *36*, 1333.
[8] K. S. Siow, *J. Alloys Compd.* **2012**, *514*, 6.
[9] Y. H. Mei, G. Chen, Y. J. Cao, X. Li, D. Han, X. Chen, *J. Electron. Mater.* **2013**, *42*, 1209.
[10] M. Y. Li, Y. Xiao, Z. H. Zhang, J. Yu, *ACS Appl. Mater. Interfaces* **2015**, *7*, 9157.
[11] P. Gadaud, V. Caccuri, D. Bertheau, J. Carr, X. Milhet, *Mater. Sci. Eng. A* **2016**, *669*, 379.
[12] X. M. James Carr, P. Gadaud, S. A. E. Boyer, G. E. Thompson, P. Lee, *J. Mater. Process. Technol.* **2015**, 19.
[13] X. Milhet, A. Nait-Ali, D. Tandiang, Y. J. Liu, D. Van Campen, V. Caccuri, M. Legros, *Acta Mater.* **2018**, *156*, 310.
[14] T. Suzuki, T. Terasaki, Y. Kawana, D. Ishikawa, M. Nishimura, H. Nakako, K. Kurafuchi, *IEEE Trans. Device Mater. Reliab.* **2016**, *16*, 588.
[15] S. T. Chua, K. S. Siow, *J. Alloys Compd.* **2016**, *687*, 486.
[16] F. Yu, J. Z. Cui, Z. M. Zhou, K. Fang, R. W. Johnson, M. C. Hamilton, *IEEE Trans. Power Electron.* **2017**, *32*, 7083.
[17] S. Bezuk, *Additional Conf. (Device Packaging, HiTEC, HiTEN, & CICMT)*, **2014**.
[18] S. Seal, M. D. Glover, H. A. Mantooth, presented at *30th Annual IEEE Applied Power Electronics Conference and Exposition (APEC)*, IEEE, Charlotte, NC, March **2015**.
[19] M. Dierolf, A. Menzel, P. Thibault, P. Schneider, C. M. Kewish, R. Wepf, O. Bunk, F. Pfeiffer, *Nature* **2010**, *467*, 436.
[20] M. Holler, A. Diaz, M. Guizar-Sicairos, P. Karvinen, E. Farm, E. Harkonen, M. Ritala, A. Menzel, J. Raabe, O. Bunk, *Sci. Rep.* **2014**, *4*, 3857.
[21] A. Diaz, P. Trtik, M. Guizar-Sicairos, A. Menzel, P. Thibault, O. Bunk, *Phys. Rev. B* **2012**, *85*, 020104.
[22] M. Holler, M. Guizar-Sicairos, E. H. R. Tsai, R. Dinapoli, E. Muller, O. Bunk, J. Raabe, G. Aeppli, *Nature* **2017**, *543*, 402.
[23] K. S. Siow, *J. Electron. Mater.* **2014**, *43*, 947.
[24] S. Sakamoto, S. Nagao, K. Suganuma, *J. Mater. Sci. Mater. Electron.* **2013**, *24*, 2593.
[25] H. J. Lee, J. Yu, *J. Electron. Mater.* **2008**, *37*, 1102.
[26] G. Muralidharan, D. N. Leonard, H. M. Meyer, *J. Electron. Mater.* **2017**, *46*, 4085.
[27] W. C. Mallard, R. F. Bass, L. M. Slifkin, A. B. Gardner, *Phys. Rev. B* **1963**, *129*, 617.
[28] O. Kubaschewski, *Trans. Faraday Soc.* **1950**, *46*, 713.
[29] M. H. Greene, A. P. Batra, R. C. Lowell, R. O. Meyer, L. M. Slifkin, *Phys. Status Solidi A* **1971**, *5*, 365.
[30] E. Gonzalez, J. Arbiol, V. F. Puntes, *Science* **2011**, *334*, 1377.
[31] R. O. Meyer, *Bull. Am. Phys. Soc.* **1969**, *14*, 389.
[32] C. Kittel, *Introduction to Solid State Physics*, Wiley, Hoboken, NJ **2005**.
[33] Y. C. K. Chen-Wiegart, F. E. Camino, J. Wang, *ChemPhysChem* **2014**, *15*, 1587.
[34] M. Holler, J. Raabe, R. Wepf, S. H. Shahmoradian, A. Diaz, B. Sarafimov, T. Lachat, H. Walther, M. Vitins, *Rev. Sci. Instrum.* **2017**, *88*, 113701.
[35] M. Holler, J. Raabe, A. Diaz, M. Guizar-Sicairos, C. Quitmann, A. Menzel, O. Bunk, *Rev. Sci. Instrum.* **2012**, *83*, 073703.

© 2020 WILEY-VCH Verlag GmbH & Co. KGaA, Weinheim